Dissolution–precipitation kinetics during C3S hydration: A holographic interferometry study

Ludovico Mascarin, Luca Valentini, Gilberto Artioli, Maria Chiara Dalconi, Jean Colombani

▶ **To cite this version:**

Ludovico Mascarin, Luca Valentini, Gilberto Artioli, Maria Chiara Dalconi, Jean Colombani. Dissolution–precipitation kinetics during C3S hydration: A holographic interferometry study. Cement and Concrete Research, 2023, 173, pp.107252. 10.1016/j.cemconres.2023.107252 . hal-04210396

HAL Id: hal-04210396
https://hal.science/hal-04210396

Submitted on 18 Sep 2023

HAL is a multi-disciplinary open access archive for the deposit and dissemination of scientific research documents, whether they are published or not. The documents may come from teaching and research institutions in France or abroad, or from public or private research centers.

L'archive ouverte pluridisciplinaire **HAL**, est destinée au dépôt et à la diffusion de documents scientifiques de niveau recherche, publiés ou non, émanant des établissements d'enseignement et de recherche français ou étrangers, des laboratoires publics ou privés.

Distributed under a Creative Commons Attribution 4.0 International License

Dissolution-precipitation kinetics during C_3S hydration: a holographic interferometry study

Ludovico Mascarin[a,*], Luca Valentini[a], Gilberto Artioli[a], Maria Chiara Dalconi[a], Jean Colombani[b]

[a] *Department of Geosciences, University of Padua, via Gradenigo 6, Padua, Italy*
[b] *Institut Lumière Matière, Université de Lyon, Université Claude Bernard Lyon 1, CNRS UMR 5306, campus de la Doua, F-69622, Villeurbanne, France*

Abstract

Tricalcium silicate C_3S has been widely employed in model systems to interpret the complex mechanisms of cement hydration. The present study aims at providing an accurate description of the dissolution rate of C_3S by implementing a new approach based on holographic interferometry. We propose a protocol that allows the measurement of the pure dissolution rate constant of the C_3S phase by experiments performed in supersaturated conditions with respect to C–S–H. In these experiments, a flat polycrystalline surface of C_3S was monitored in a quiescent solution. The amount of calcium released within the holographic cell was measured and the aqueous solution composition was constrained to the C–S–H stoichiometry at the interface. An equilibrium approach was applied to assess interfacial pH, saturation indexes, and C–S–H precipitation at the experimental conditions. Providing the rate constant allowed tracing the rate law of the pure dissolution of C_3S from far to close-to-equilibrium conditions.

Keywords: Cement hydration, Tricalcium silicate, C–S–H, Holographic interferometry, Dissolution rate constant

*Corresponding author
Email addresses: ludovico.mascarin@gmail.com (Ludovico Mascarin), luca.valentini@unipd.it (Luca Valentini), gilberto.artioli@unipd.it (Gilberto Artioli), mariachiara.dalconi@unipd.it (Maria Chiara Dalconi), jean.colombani@univ-lyon1.fr (Jean Colombani)

1. Introduction

Tricalcium silicate (Ca_3SiO_5) controls Portland cement hydration kinetics and properties of the cement binder at early age. Therefore, tricalcium silicate, referred to as C_3S by following the cement chemistry notation (C = CaO and S = SiO_2), has been widely employed as a model phase to interpret the complex mechanisms of cement hydration. First principle calculations based on density functional theory (DFT) showed that oxygen atoms not covalently bound to silicon atoms and ionically bound to calcium atoms are the source of the high reactivity of the C_3S phase [1]. In light of the above, the coordination number of the surface calcium ions also plays a significant role in surface reactivity.

An electrical double layer forms on the surface of the C_3S phase upon contact with the mixing water and the hydration of C_3S begins with the dissociative adsorption of water molecules on the mineral surfaces [2]. In the first layer, the oxygen ions from dissociated water molecules adsorb on calcium ions and weaken the Ca-O bonds on the mineral surface [3]. Pustovgar et al. [4] have experimentally shown the hydroxylated state of the surface of C_3S through $^{29}Si\{^1H\}$ cross-polarization (CP) magic-angle-spinning (MAS) NMR measurements.

The surface of C_3S can be seen as formed by Ca^{2+}, OH^- and $H_4SiO_4^0$ species, the latter formed by protonation of monomeric silicate ions. Deprotonation of $H_4SiO_4^0$ species varies the surface charge and may alter mineral-water interactions [5]. In general, $H_3SiO_4^-$ species are stable above pH 9.8 and below pH 13.2. In this frame, although the detachment of calcium ions is energetically favorable compared to silicon ions and the interface may be prone to multiple reactions upon wetting, C_3S may dissolve stoichiometrically with Ca:Si = 3:1.

The hydration proceeds through dissolution, diffusion of the chemical species in aqueous solution, nucleation, and growth of the hydration product. The reaction of C_3S in water leads to the precipitation of the calcium-silicate hydrate phase, or C–S–H by adopting the cement chemistry notation (H = H_2O and hyphens denote a variable stoichiometry), which primarily conveys cohesion and mechanical properties during cement setting and hardening. Subsequently, the

continuous increase of Ca concentration in solution, due to the stoichiometry difference between C_3S and C–S–H, leads to the precipitation of portlandite (CH).

The nanostructure of the C–S–H phase has been commonly described by models based on dreierkette silicate chains [6, 7, 8]. It presents a disordered layer structure that can entrap water in the interlayer space that separates the calcium silicate sheets as well as into micropores [9, 10]. Following the notation used in ^{29}Si NMR spectroscopy, where silicon tetrahedra are classified as monomers (Q^0 silicate species) and oligomers (Q^n silicate species), the precipitation of the C–S–H phase results from the polymerization of Q^0 formed by dissolution of C_3S to build Q^1 and Q^2 units. A key feature of the C–S–H phase is the variable Ca/Si ratio as a function of the solution composition during the hydration.

The process acting as a rate-limiting step during the hydration of C_3S is still a matter of debate and many authors highlighted the role of the initial slow reaction stage of C_3S, usually called induction period. If on the one hand the number of initial C–S–H nuclei may control the length of the induction period during the hydration of the C_3S phase [11], on the other hand, by following the dissolution theory [12], the nature and dynamics of the surface defects controls the kinetics of the release of matter in the solution. Evidence of the link between etch pit nucleation rate and dissolution rate of C_3S was reported by Juilland and Gallucci [13].

The dissolution rate of a mineral in aqueous solution can be measured through batch experiments using crushed particles [14] or resorting to rotating disk set-ups using polished surfaces [15]. In typical dissolution protocols, the granular solid dissolves in a stirred batch and the dissolution rate is calculated from the time evolution of the average batch concentration, using for example an inductively coupled plasma (ICP) spectrometer. Other devices use flow-through cells, where the dissolution rate is obtained from the observation of the dissolving surface measured ex-situ by vertical scanning interferometry (VSI) or in-situ by atomic force microscopy (AFM) [16]. In any case, the calculated rate is a combination of the dissolution rate at the grain-liquid interface,

the diffusion rate within the mass-transport boundary layer developing around the grain, and the advection rate of the dissolved species [17].

These techniques, batch measurements [18, 19] as much as flow-through cells [13, 20, 21], have already been used successfully to the study C_3S dissolution.

Nevertheless, in all these techniques, as the solid dissolves in a stirred or flowing solution, a diffusive contribution, taking place in the vicinity of the reacting surface, sums up to the pure dissolution rate, depending on the intensity of the flow, which may likely affect the results [13]. Therefore, in classical dissolution measurements assumptions have to be made about the limiting step of the kinetics (diffusion-limited *vs* reaction-limited).

The present study aims at providing an accurate description of the dissolution rate of C_3S by implementing a new approach based on holographic interferometry, a method already used to measure the dissolution rate of gypsum and anhydrite [22] and the corrosion kinetics of hardened cement [23]. Here, we propose a protocol that allows the measurement of the pure dissolution rate constant of C_3S by analyses performed in supersaturated conditions with respect to C–S–H that do not necessitate assuming the experiment as reaction-driven or transport-driven. Our experiments were carried out in a stagnant solution, by monitoring in real-time the concentration of calcium species released within a holographic cell from a flat polycrystalline surface of C_3S, and separately quantifying the diffusive contribution. This paper, by a detailed analysis of both the fluid mechanics and the surface chemistry at our particular experimental conditions, provides new measurements of the dissolution rate of C_3S from far to close-to-equilibrium conditions and aims at contributing to the development of models of cement hydration kinetics.

2. Materials and methods

The C_3S used in this study (triclinic polymorph with a B.E.T. specific surface area of 0.4 m^2/g) was provided by Mineral Research Processing (Meyzieu, France) [24]. C_3S powder was placed between the two anvils of a hand press

(Quick Press KBr Pellet Kit) and the pressure was applied by a handshake to the handle of the press for 15 min. Platelets of pressed C_3S powder with a diameter of 7 mm and a height of 0.5 mm were obtained by this procedure. The grain size was small enough for the surface of these samples to be quasi-continuous. Therefore, the polycrystalline surface was treated as a topographically flat interface of a single crystal with a geometric surface area of $\sim$38.5 mm^2.

Previous dissolution experiments, using flow-through cells, have been performed on polished cross-sections of minerals after embedding the sample in a thermosetting polymer [13, 20] or solid-state sintering [25, 26]. However, our methodology is extremely sensitive to any change in the refractive index possibly caused by foreign agents, e.g. solvents released by an epoxy resin. While these chemicals are rapidly evacuated in a flow-through cell, these may accumulate in a closed cell and possibly induce unwanted artefacts. For this reason, despite the brittleness of the platelets, our C_3S samples were merely compacted without embedding. The samples, when carefully handled, could be introduced into the holographic cell with no need for a sintering process that may modify porosity and surface properties.

These platelets were hydrated in a transparent cell with a total volume of 4 cm^3, either in deionized water or in solutions of 0.6 mM $Ca(OH)_2$. Calcium hydroxide solutions were kept under gentle stirring and left to cool before their introduction within the holographic cell. The concentration of $[CaO]_{aq}$ into the initial solution was very small compared to other studies [13, 18]. The choice was owed to the impracticability to fully isolate the cell from the external environment during the experiments. Therefore, only solutions with initial concentrations below (or close) the solubility of $CaCO_3$ in condition of atmospheric CO_2 exposure can be studied. Each experiment was repeated at least three times to estimate the standard deviation.

2.1. Holographic interferometry

Whereas standard interferometry generates interferences between objects separated in space, holographic interferometry generates interferences between

objects separated in time [27]. This was achieved by the acquisition of a reference hologram of a transparent object, here a spectroscopic cell containing the solution, illuminated by green laser light. Subsequently, the analyzed sample, i.e. the C_3S platelet, was introduced at the bottom of the cell, and new digital holograms of the system (cell + sample) were recorded at regular intervals. The interferences between each hologram and the reference hologram were then numerically computed. The interferograms display the evolution of the refractive index δn between the reference hologram (pure solution) and the hologram at time t (solution + dissolved C_3S). As the solid dissolves and the ionic species migrate upward by diffusion, the refractive index change is visualized as a series of ascending horizontal fringes (Figure 1).

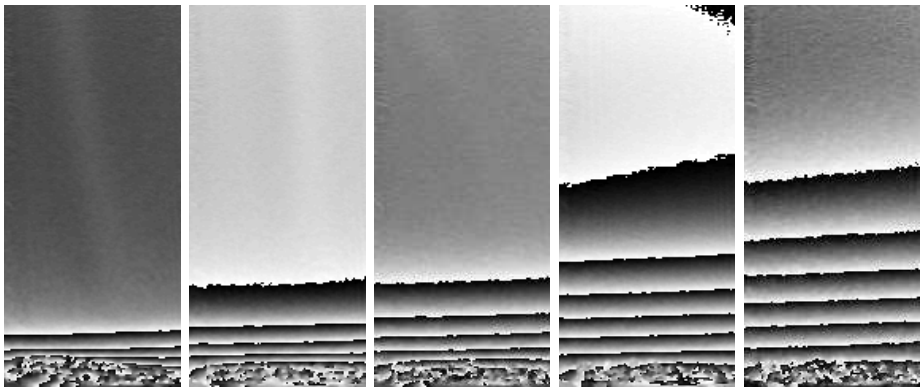

Figure 1: Digital holographic interferograms of the dissolution of the C_3S platelet in deionized water at different times from left to right (10, 25, 45, 120, and 220 min) after the introduction of the sample at the bottom of the cell. The total cell width and length are 10 mm and 40 mm respectively, and the displayed interferograms are 5.9 mm wide and 12.9 mm high. The pixel size is 12 μm.

Knowing the evolution $\partial n/\partial c$ of the refractive index of the solution n with the concentration of dissolved species it is possible to compute the spatial variation of the ionic species concentration from the solid-liquid interface toward the top of the cell. The conversion of the spatial evolution of the refractive index

δn inside the cell to spatial change of concentration δc follows Equation 1.

$$\delta c = \frac{\delta n}{(\partial n / \partial c)} \tag{1}$$

The quantification of the absolute ionic concentration requires a reference value, therefore we have assumed that the solution at the top of the cell was still pure ($c_{\text{top}} = 0$ in pure water, and $c_{\text{top}} = 0.6$ mM of Ca^{2+} in calcium hydroxide solutions) and the concentrations were computed from this position. Therefore, the concentration in all points was $c = c_{\text{top}} + \delta c$. The experiments were stopped as soon as a fringe reached the top of the cell.

Once converted the refractive index change to concentration change (see Equation 1), the latter was averaged over the horizontal axis perpendicular to the laser beam by assuming a one-dimensional phenomenon, and $\delta c(z,t)$ was calculated as a function of the vertical coordinate within the cell (z-axis) and the time t. An example of the evolution of the ionic concentration along the vertical axis at different times is shown in Figure 2.

A theoretical expression of the $c(z,t)$ curves was derived by solving Fick's second law by assuming a semi-infinite medium upward and continuous matter supply at the bottom following a first-order dissolution rate law. Indeed, as the sample is never completely dissolved at the end of the experiment, an infinite reservoir of solid can be assumed. The solution of Fick's equation with these boundary conditions [28] is displayed in Equation 2:

$$\delta c(z,t) = c_{\text{sat}} \left[\text{erfc}\left(\frac{z}{2\sqrt{Dt}} \right) - \exp\left[\frac{k(s_{\text{r}}/s_{\text{d}})z}{D\rho c_{\text{sat}}} + \left(\frac{k(s_{\text{r}}/s_{\text{d}})}{D\rho c_{\text{sat}}} \right)^2 Dt \right] \times \text{erfc}\left[\frac{z}{2\sqrt{Dt}} + \frac{k(s_{\text{r}}/s_{\text{d}})}{D\rho c_{\text{sat}}} \sqrt{Dt} \right] \right] \tag{2}$$

where the erfc is the complementary error function, k is the dissolution rate constant, D is the diffusion coefficient, s_{r} is the surface area, s_{d} the horizontal

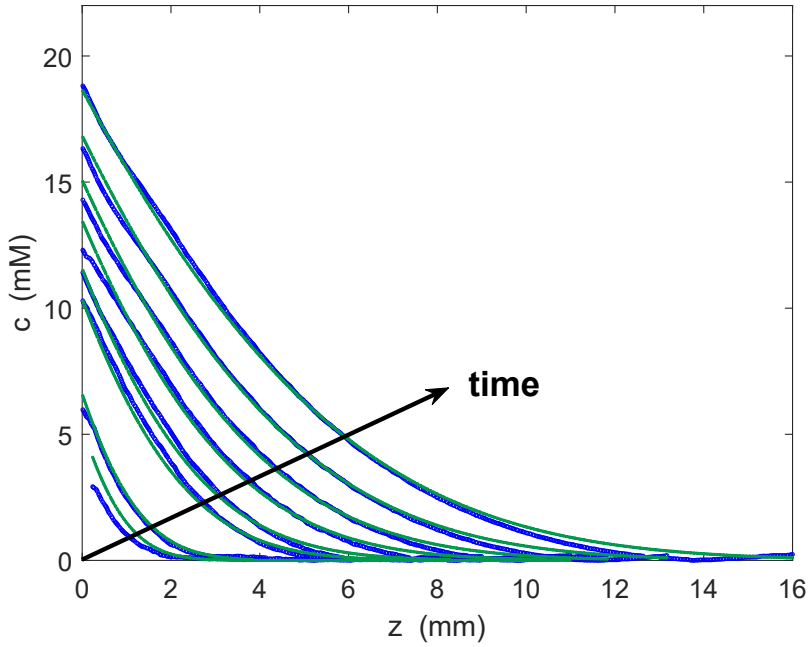

Figure 2: Time-variation of the calcium concentration as a function of the vertical position z during the dissolution of a C_3S sample lying at z = 0 in pure water. The interfacial concentrations evolve over time along the ordinate axis from the bottom (first hydration time) to the top (last hydration time). Each experimental curve (in blue) progressively displaces from the interface (z = 0) to the top of the cell according to the diffusion of the ionic species. The blue curves were recorded at 5, 10, 30, 30, 40, 60, 85, and 170 min elapsed time since the introduction of the sample in the solution. The green curves correspond to the best fit of the experiments with the theoretical law (Equation 2).

section of the cell, ρ is the density of the solution and c_{sat} is the concentration at saturation. In our case, s_r is a geometric surface area that neglects the surface roughness and the presence of defects at the atomic scale.

A typical fit of the experimental data with this analytic expression was shown in Figure 2. The agreement between the experimental data and the theoretical law was good in all our experiments, which is a posteriori validation of our choice of the diffusion equation and of the first-order reaction used as boundary condition. The fitting of the holographic concentration curves by using Equation

2 provides the values of k, D and c_{sat}. These three parameters are independent of space, time, and concentration. Therefore, one single value for each of them is obtained by fitting the whole dataset of a given experiment with Equation 2.

Compared to classical dissolution devices, holographic interferometry presents the advantage that the solid dissolves in a quiescent solution, no stirring is imposed on the liquid, and the concentration of ionic species is monitored in real-time at any position within the dissolution cell. The sample surface was directly monitored and the interfacial concentration of the ionic species $c(z = 0, t)$ was extrapolated. With regard to the kinetics, no assumption such as diffusion-limited, reaction-limited, or a combination of both is required because the contribution of diffusion is quantitatively measured. Hence, the pure dissolution rate is accessed free from mass transport and taking into account the precipitation as will be discussed hereafter.

3. Results and discussion

3.1. Surface morphology

The nucleation of the C–S–H phase is a heterogeneous phenomenon that occurs at the surface of the dissolving C_3S grains. The fitting of experimental data by means of Boundary Nucleation and Growth (BNG) models, which assume heterogeneous nucleation on the substrate of tricalcium silicate, indicated that the nucleation of the C–S–H phase is almost spontaneous [29, 30]. Nucleation times of the order of minutes or seconds were also reported by applying the classical nucleation theory [31].

Under the stagnant conditions used during the holographic experiments, the supersaturation with respect to the hydration product may be higher inside the etch pits than on the rest of the surface. Indeed, crystal dissolution proceeds with the opening of holes from surface defects [12]. In our conditions, far from the equilibrium with respect to C_3S, etch pits may represent preferential sites for the nucleation of C–S–H [32]. Moreover, the null or very low concentration of

$[CaO]_{aq}$ into the initial solution may produce a higher number of initial C–S–H nuclei [11]. This condition may favor the rapid growth of the C–S–H phase.

In order to provide a correct interpretation of our results, we performed SEM analyses of hydrated C_3S surfaces at the end of some holographic interferometry experiments, with the aim of assessing the possible precipitation of C–S–H. As shown in Figure 3, the surface of the C_3S grains was partially covered by characteristic C–S–H needles [19, 33], thus suggesting rapid precipitation of this reaction product, whereas portlandite was not observed in the investigated time interval (220 min).

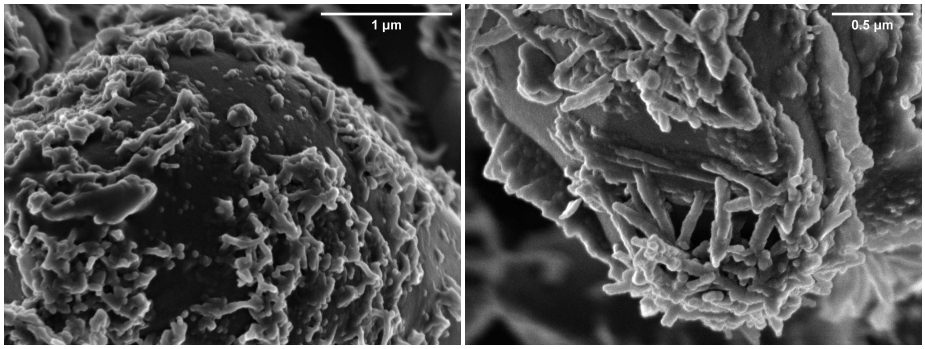

Figure 3: SEM micrograph of the surface of the hydrated platelet of C_3S at 45 min (left) and 120 min (right). The C–S–H needles are distributed on the surface of the hydrated sample. SEM micrographs were collected on dried surfaces coated with a layer of graphite. The secondary electron images were acquired with a TESCAN Solaris FEG-SEM at low voltage (2 KeV) to avoid surface charging and high vacuum mode.

3.2. Index of refraction

The central quantity that is needed to obtain the variation of the concentration c in the cell (see Figure 2) is the evolution of the refractive index n of the solution with the concentration of c ions it contains. Here, holointerferometric measurements were combined with analyses by inductively coupled plasma atomic emission spectroscopy (ICP-AES) in order to determine the unknown value of $\partial n/\partial c$.

Holographic curves were collected at various total times (5, 15, 30, 45, 75, and 120 min) in independent experiments. The refractive index change $\delta n(z)$ along the cell (z vertical position) was recorded by the interferometric device for these six different times. The average value $\delta n_{\mathrm{avg}}(t)$ in the whole cell was computed from the integral of the holographic curve at the mentioned hydration times. Afterwards, the average concentrations of calcium $c_{\mathrm{Ca}}(t)$ and silicon $c_{\mathrm{Si}}(t)$ at the end of the six experiments were measured by ICP-AES. The time evolution of their concentration in the cell during the hydration of C_3S is displayed in Figure 4. We stress that the cell where we measured the average Ca and Si concentrations is a system out of equilibrium where the species are spatially distributed. Therefore, these data can not be located in an averaged $c_{\mathrm{Ca}} - c_{\mathrm{Si}}$ diagram [19].

The aqueous solution in the cell was significantly enriched in Ca, roughly one order of magnitude more than Si. This gap between the concentration of Ca and Si may have two origins: the incongruent dissolution of C_3S, which may change the Ca:Si ratio of dissolution compared to how expected from the mineral stoichiometry, or the precipitation of the C–S–H phase, which may control the evolution of the ionic concentration mainly by silicon depletion from the aqueous phase.

In virtue of our SEM observations, we assumed a congruent dissolution of C_3S, driven by the degree of saturation, which occurred simultaneously with the precipitation of C–S–H. Regardless of the saturation state, the precipitation of C–S–H consumes less than the 3 moles of Ca^{2+} released by dissolution of C_3S, thus leading to a continuous increase of Ca in solution, while most of the silicon is incorporated into the C–S–H phase during the hydration. Therefore, we considered that the variation of the refractive index was solely associated with the change of concentration in Ca, and a link between $\delta n_{\mathrm{avg}}(t)$ and the Ca concentration was established. The variation of the refractive index with Ca concentration was calculated for each of the investigated times and the average value with the relative standard deviation was $\partial n/\partial c_{\mathrm{Ca}} = \delta n_{\mathrm{avg}}/c_{\mathrm{Ca}} = 0.023 \pm$

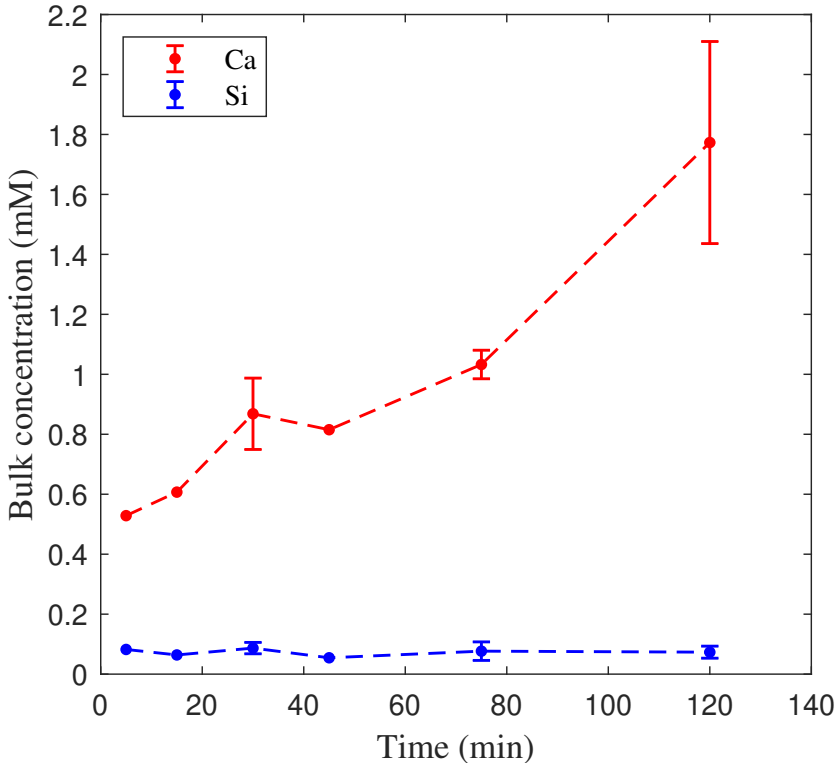

Figure 4: Average concentration of calcium and silicon in the holointerferometric cell. Platelets of C_3S were hydrated in deionized water and the final composition of the solution was analyzed by ICP-AES at different times. Data were reported with the measurement error due to the dissolving surface area of the C_3S discs.

0.005 L/mol. In the following, all the calcium concentrations were computed according to Equation 1, provided that no fringe reached the top of the cell (see Section 2.1). To help clarify, c stands for the calcium concentration in Figure 2.

3.3. Dissolution rate constant of C_3S

To estimate the number of calcium ions liberated in the cell and not captured by the C–S–H precipitation, we turned to the stoichiometry of the hydration product. As stated in Section 3.2, we have discarded the assumption of incongruent dissolution of C_3S and we considered that each C_3S mole released three

moles of Ca^{2+} along the reaction $Ca_3SiO_5 + 5\,H_2O \rightarrow 3\,Ca^{2+} + H_4SiO_4 + 6\,OH^-$. Moreover, the SEM analysis showed that CH did not precipitate during our experiments. Thus, the matter conservation imposes $3 = x + z$, being z the number of moles of Ca^{2+} in solution per mole of dissolved C_3S and x the number of moles of Ca^{2+} in one mole of C–S–H (see equilibrium reaction in [34]). In this frame, the question of the value of x, i.e., the Ca/Si ratio of the C–S–H phase, arose spontaneously.

As mentioned in Section 1, the stoichiometry of the C–S–H evolves during the hydration process. A feature of the C–S–H phase is the replacement of bridging silicate tetrahedra with calcium site and of silicate dimers with hydroxyl groups [35]. This mechanism may account for stabilizing the structure of the C–S–H phase at a high Ca/Si ratio during the hydration. Allen et al. [10] determined the mean formula of the nanoscale C–S–H phase in hydrated cement through the aid of small-angle scattering techniques. The mean Ca/Si ratio of the C–S–H phase within hydrated Portland cement pastes was reported to be about 1.7 [36].

According to water content, saturation state, lime concentration in solution, and hydrodynamic experiment conditions, the hydration of C_3S may require time to stabilize the composition of the C–S–H phase. The ideal solid solution model developed by Bullard and Scherer [37] predicts the composition of the C–S–H phase as a function of the aqueous solution composition during hydration. The model is based on three C–S–H end-members with Ca/Si ratios equal to 0.8, 1.0, and 1.8. These three end-members were chosen as the best combination to fit the solubility data [38] and to approximate the Ca/Si ratios of C–S–H reported by Haas and Nonat [39].

We have used the reaction equilibria of these three end-members to determine the total supersaturation with respect to C–S–H. Through the aid of Minteq [40], we increased the concentration of C_3S step-by-step until reaching the saturation of the solid solution. This condition was achieved by dissolving 0.5 mM of C_3S. The total activity of calcium species at equilibrium in solution was 1.14 mM. This calculation allowed the estimation of the point at which sat-

uration with respect to C–S–H was reached within our experimental conditions. The evolution in calcium concentration at the solid-liquid interface, where the dissolution-precipitation reactions occur, is displayed in Figure 5.

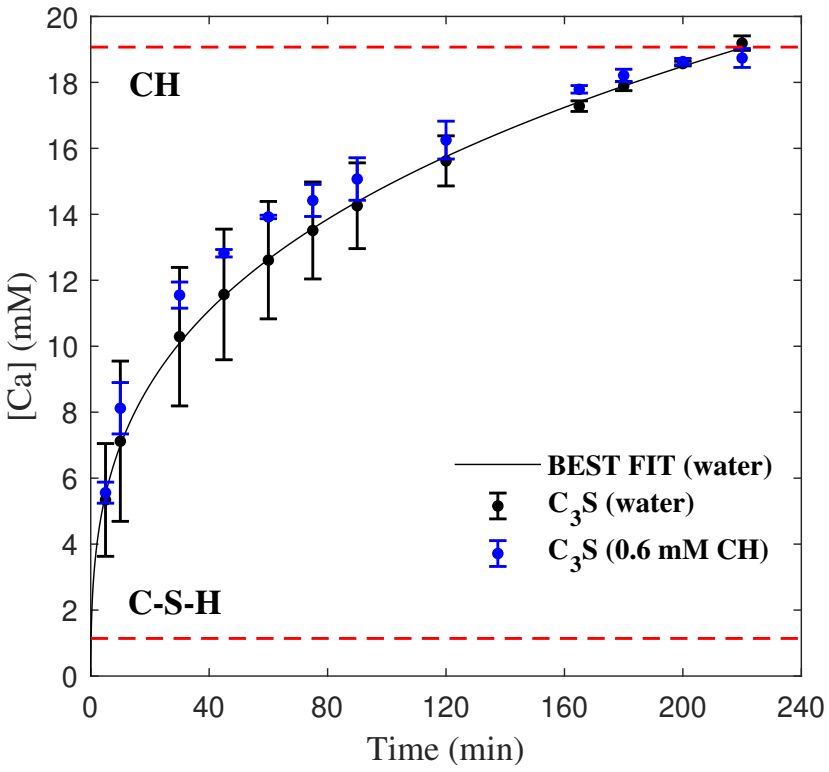

Figure 5: Concentration of calcium *versus* time at the solid-liquid interface during the dissolution of the C_3S platelet in deionized water and lime solution. Errorbars represent the standard deviation calculated from three repeated measures. The best fit of the average interfacial concentration (Equation 2 with $z = 0$) of the experiments in deionized water was illustrated with a black curve. The solubility of C–S–H and CH were calculated with the aid of Minteq [40] and depicted with red dashed lines.

The range of interfacial concentration approached the solubility of CH after 220 min of hydration, i.e. at the end of our experiments. For this reason, the calcium concentration was free to increase and no local sink was observed.

Then, following the model proposed in [37], we correlated the amount of calcium released in solution at the interface with the C–S–H stoichiometry. In such a way, we determined the x moles of Ca into C–S–H and, by mass balance, the z moles of Ca into the solution (see Section 3.4). Adopting this strategy we were able to pass from the dissolution rate constant experimentally determined through holography, which was based on the calcium release rate, to the dissolution rate constant of the C_3S phase according to Equation 3:

$$k_{C3S} = \frac{\sum \left(\frac{k}{z}\right)}{N} \tag{3}$$

where the k was weighted on the number z of moles of calcium in solution per mole of dissolved C_3S and N was the number of holographic curves for each experiment. The mean dissolution rate constant of C_3S in pure water was $k_{C3S} = 19.8 \pm 4.4$ μmol·m^{-2}·s^{-1}. The dissolution rate constant in the lime solution was inside the experimental uncertainty. We stress that this value is the pure thermodynamic coefficient, free from any other phenomenon, such as mass transport.

The dissolution rate constant k_{C3S} calculated from our experiments is in agreement with the 'first dissolution rate' obtained from VSI measurements by Kumar et al. [41]. Specifically, the rate obtained with an optical profilometer was measured through rain-drop experiments that considered the first seconds contact between the mineral surface and deionized water and repeated cycles using the virgin solvent. The value of 25.7 μmol·m^{-2}·s^{-1} from [41], which relied on topographical changes with time in the average height of the particles over a scanning area, should be a good approximation of the dissolution rate constant. The agreement with our value of k_{C3S}, as well as the comparability with dissolution rates provided by other VSI measurements [13, 20, 21], contributes to the validation of our methodology.

In light of the progress in geochemistry, the changes in the reactive surface area during the hydration have been long debated [34, 42, 43]. Pustovgar et al.

[4] have shown that hydroxylated Q^0 silicate species were predominant during the induction period of the hydration and persisted constantly up to the beginning of the deceleration regime at longer times of hydration. These silicate monomers were not part of the polymerized structure of the C–S–H phase.

Therefore, we considered that the coverage of the hydration product may not dramatically reduce the reactive surface area, as inferred by the distribution of the above mentioned hydroxylated Q^0 silicate species, during our experiments. We support the idea that, as long as the reactions occur on the substrate, the loss of available surface may in part be compensated by the surface active mechanism such as local etching [32]. For this reason, the surface area used in this study was the geometric surface of the C_3S discs (see Section 2).

In a recent work performed with the aid of fast nano X-ray computed tomography, it has been assessed that different particle sizes of C_3S grains may dissolve at a similar rate per surface area [59]. This consideration, which appears less aligned with a dissolution driven by particle sizes [60], strengthens the consensus towards our surface area treatment. On the other hand, spatial dissolution rates obtained with the aid of beamline techniques, for instance by combining microstructure evolutions with phase-selective signals [61], beyond not comparable with our methodology since never representative of far-from-equilibrium conditions with respect to C_3S, may vary with the particle sizes and the stage of cement hydration.

The thermodynamic framework described in the next section illustrates the conditions under which our holographic experiments were carried out.

3.4. Interfacial pH and saturation state

An equilibrium approach was applied to assess the saturation state at which our experiments were carried out. This approach started with the designation of model points. In particular, five calcium concentrations of the aqueous solution included within the range of our experimental points were selected. These molar concentrations corresponded to five Ca/Si ratios of the C–S–H phase [37]. A third relationship with the time was defined by knowing the empirical law that

connected our experimental points (black dashed line in Figure 5). In doing so, we got the time at which the model points presented the model $(Ca/Si)^{CSH}$. The model points' conditions describing the time the aqueous solution was at equilibrium with a particular C–S–H composition is reported in Table 1.

Table 1: List of model points' conditions.

Time (min)	$[Ca]^{aq}$ (mM)	$(Ca/Si)^{CSH}$
6.5	6.0	1.1
14.4	7.9	1.2
28.3	9.9	1.3
55.2	12.3	1.4
111.8	15.4	1.5

An empirical law that links the Ca/Si ratio of C–S–H to the equilibrium constant of reaction has been reported by Blanc et al. [44]. Inspired by this work we assigned a reaction stoichiometry to the five C–S–H end-members used as model points and we solved the equilibrium. The thermodynamic equilibria are reported in Table 2.

Table 2: Equilibrium reaction and solubility product of the five C–S–H end-members.

REACTION	$\log(K_{SP}^{CSH})$
$Ca_{1.1}SiO_2(OH)_{2.2}(H_2O) \rightarrow 1.1Ca^{2+} + H_3SiO_4^- + 1.2OH^-$	-9.44
$Ca_{1.2}SiO_2(OH)_{2.4}(H_2O) \rightarrow 1.2Ca^{2+} + H_3SiO_4^- + 1.4OH^-$	-10.14
$Ca_{1.3}SiO_2(OH)_{2.6}(H_2O) \rightarrow 1.3Ca^{2+} + H_3SiO_4^- + 1.6OH^-$	-10.80
$Ca_{1.4}SiO_2(OH)_{2.8}(H_2O) \rightarrow 1.4Ca^{2+} + H_3SiO_4^- + 1.8OH^-$	-11.44
$Ca_{1.5}SiO_2(OH)_{3.0}(H_2O) \rightarrow 1.5Ca^{2+} + H_3SiO_4^- + 2.0OH^-$	-12.05

In order to determine the number of OH^- ions, and thus the interfacial pH, and partition the calcium species, a system composed of four equilibria was solved for each C–S–H composition. The system included the equilibrium for C_3S, the equilibrium for C–S–H, the chemical speciation of Ca, and the total amount of Ca at equilibrium in solution (see Table 1). The solubility product of

C_3S extrapolated from dissolution rates was used [18]. In our system, we considered a deprotonated surface formed by $H_3SiO_4^-$ species. The equilibrium of C_3S was computed by considering the equilibrium for the silicic acid in Equation 4.

$$[H_4SiO_4^0] = \frac{[H_3SiO_4^-]}{[OH^-]} \cdot 10^{-4.16} \tag{4}$$

Through this operation, we simplified the system by getting rid of the $H_3SiO_4^-$ species. Indeed, only a tiny quantity of silicon was expected to lie on the interface compared to calcium ions. We thus initially neglected the influence of silicon on the interfacial pH. The mass balance was solved in the system below:

$$\begin{cases} [Ca^{2+}]^3[H_3SiO_4^-][OH^-]^5 = 1.4 \cdot 10^{-18} \\ [Ca^{2+}]^r[H_3SiO_4^-][OH^-]^s = t \\ [CaOH^+] = [Ca^{2+}][OH^-] \cdot 10^{1.3} \\ [CaOH^+] + [Ca^{2+}] = c \end{cases} . \tag{5}$$

where r and s are stoichiometric coefficients of equilibrium, t is the equilibrium constant (see Table 2), and c is the total calcium concentration in solution (see Table 1). The final graph of the evolution of the interfacial pH is shown in Figure 6 (right).

The pH of fresh and hardened cement pastes, among the available practices [45], has been generally obtained by pore solution extraction [46, 47], and has been measured either with a calibrated pH electrode or by titration. It has been reported that the pH of Portland cement lies between 12.5 and may get above 13 [45]. The interfacial pH values obtained for the experimental points by implementing the previously described approach ranged from 10.8 and 12.3. These values took into account the coupled reactions (C_3S dissolution and C–S–H precipitation) occurring at the surface. We recall that these values did not consider the pH buffering due to the precipitation of CH during the hydration because our working concentration always remained below the CH solubility.

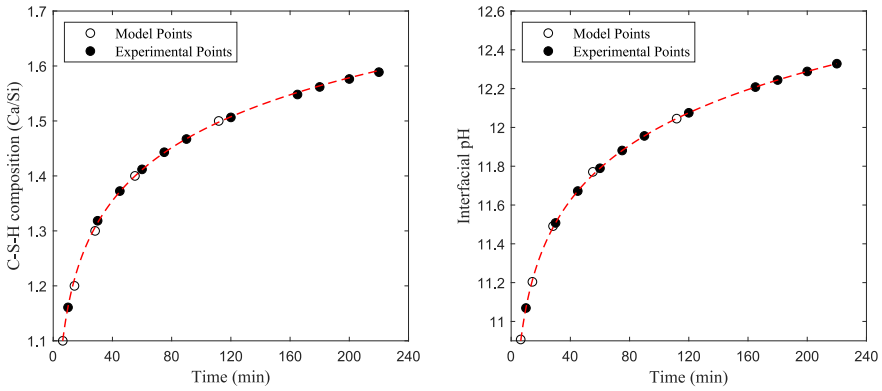

Figure 6: $(Ca/Si)^{CSH}$ *versus* time (left): model points and experimental points were used to trace a trendline; pH *versus* time (right): the best fit of the model points follows a power law and the experimental points were added to the curve.

The concentration of Ca^{2+} ions in the model points was calculated by rearranging the equilibria (see system in Equation 5). The concentration of Ca^{2+} in the model points differed from the one in the experimental points by a factor that concerned the ratio between the equilibrium of C_3S and the equilibria of the C–S–H end-members. In such a way, the concentration of Ca^{2+} in the model points took into account the coupled reactions, while the concentration of Ca^{2+} in the experimental points simply resulted from the calcium balance. This difference was used to estimate the number of interfacial $H_3SiO_4^-$ species at equilibrium. Accordingly, the average quantity of silicon species not captured by the C–S–H phase was $1.6{\cdot}10^{-4}$ mol/L. Lastly, the molar concentrations of Ca^{2+}, $H_3SiO_4^-$ and OH^- were used to compute the saturation index of C_3S, C–S–H and CH as shown in Figure 7.

The estimated index of saturation of C_3S was -8.7 at 5 minutes of hydration and approached the equilibrium at the end of our experiments. The index of saturation of CH was -3.3 at 5 minutes, and similar to C_3S, the interfacial solution composition stayed below its solubility for almost the entire length of our experiments, as already shown in Figure 5. Any slight saturation in CH toward the last investigated times is associated with our computation of

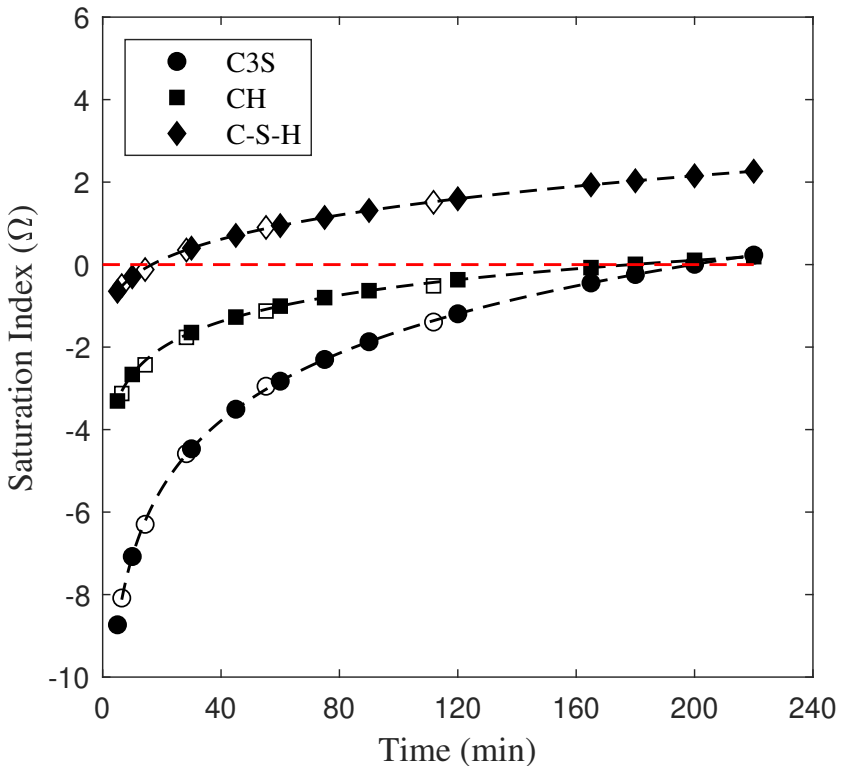

Figure 7: Evolution of the saturation index of C_3S, C–S–H, and CH. The curves included the model points (empty markers) and the experimental points (filled markers). Equilibria of C_3S and C–S–H considered Ca^{2+}, $H_3SiO_4^-$, and OH^- species. The equilibrium constant of portlandite was $K_{SP}^{CH} = \{Ca^{2+}\}_{eq} \{OH^-\}_{eq}^2 = 5.1 \cdot 10^{-6}$.

OH^- species. As regards the C–S–H phase, the evolution of the saturation index considered the variation of $(Ca/Si)^{CSH}$ during the hydration. The model predicted a slight undersaturation with respect to C–S–H up to 10 minutes of hydration. These conditions corresponded to $(Ca/Si)^{CSH}$ lower than 1.2. However, as predicted by implementing the ideal solid solution model [37], the precipitation of C–S–H may occur almost spontaneously during our experiments (see Figure 5). Therefore, the slight undersaturation with respect to C–S–H may arise out of a different C–S–H stoichiometry or a higher concentration of silicon in the aqueous solution.

Nevertheless, this strategy allowed the definition of the approximate interfacial saturation state at the hydrodynamic conditions used in this study. Following this approach, we make clearer how we succeeded in computing the pure dissolution rate of C_3S by separating the effect of C–S–H precipitation occurring at the surface of our platelets during hydration.

3.5. C–S–H precipitation

Determining the number of Ca^{2+} species, either in solution or incorporated into the C–S–H phase was possible by following the previously described approach (Section 3.3 and Section 3.4).

The molar concentration of Ca^{2+} ions within C–S–H was calculated from Equation 6:

$$Ca^{2+}_{CSH} = Ca^{2+}_{aq} \cdot \frac{x}{z} \tag{6}$$

where x and z are the moles of Ca^{2+} respectively in one mole of C–S–H and in solution.

The sum of Ca^{2+} ions released in solution and the ones used to build the C–S–H phase gave the total amount of Ca^{2+} dissolved from the C_3S surface during the hydration. The amount of $H_3SiO_4^-$ ions dissolved from C_3S and used to form C–S–H was obtained from the dissolution stoichiometry of tricalcium silicate. The total concentration of Ca^{2+} and $H_3SiO_4^-$ detached from the C_3S surface during the hydration is shown in Figure 8. The evolution of $H_3SiO_4^-$ species may approximate the precipitation of the C–S–H phase. The interfacial growth rate of C–S–H has been specifically studied in [48].

3.6. Dissolution rate law of C_3S

The standard rate law of dissolution is based on the transition state theory (TST). For instance, rate laws based on the TST have been implemented on the HydratiCA reaction-diffusion model [49] and have been used to model the rate processes during the hydration of the C_3S phase [50]. Describing a rate

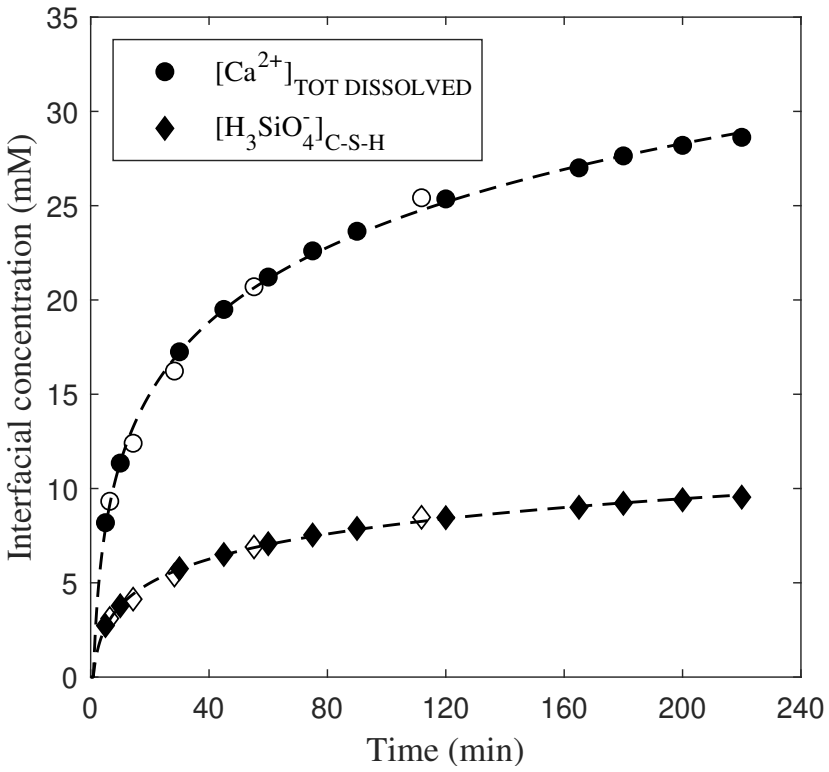

Figure 8: Total Ca^{2+} ions and $H_3SiO_4^-$ ions dissolved from the C_3S surface. The curves included the model points (empty markers) and the experimental points (filled markers).

process by resorting to the classical TST means dividing the overall rate of reaction into elementary reactions that account for the reaction mechanism. The slowest elementary reaction represents the rate-controlling step that regulates the overall rate process.

The dissolution proceeds along the minimum Gibbs free energy path. The undersaturation ($\Omega < 0$) or deviation from the Gibbs free energy of reaction ($\Delta_r G < 0$) is the driving force for the dissolution. Far-from-equilibrium conditions are characterized by a dissolution plateau. Moving toward close-to-equilibrium conditions a sharp linear decrease in the dissolution rate occurs in a nonsigmoidal fashion.

Recent studies of C_3S dissolution, inspired by the progress of the understanding of the atomic mechanisms underlying mineral dissolution, have led to the refinement of the TST. Sigmoidal functions that describe the variation of the rate with the deviation from the equilibrium have been observed for C_3S dissolution [18] and this functional form was interpreted as the signal of the presence of dissolution stepwaves generated by etch pits at the crystal surface [12]. This model argues that the walls of pre-existing pits at the crystal surface generate steps that propagate along the edges of the same atomic defects and dissolve the crystal surface layer by layer. In this frame, the sigmoidal pattern testifies the non-steady-state rate when passing from dissolution controlled by the etch pit nucleation (far-from-equilibrium) to dissolution limited by the step retreat generated by screw dislocation lines intersecting the crystal surface (close-to-equilibrium). These reaction mechanisms have been reported in cases of study on the albite feldspar [51, 52], before being successfully applied to the case of C_3S [42, 43].

The methodology used in our study has assumed a first-order dissolution rate (see Section 2.1), thus the change of the dissolution rate of C_3S from far to close-to equilibrium was traced in Figure 9 (black curve) by using Equation 7:

$$R = k_{\mathrm{C3S}} \cdot \left(1 - \frac{\Pi}{K_{\mathrm{eq}}}\right) \tag{7}$$

where k_{C3S} is the dissolution rate constant determined in this study, which is intrinsically normalized to the geometric surface area, $K_{\mathrm{eq}} = \{Ca^{2+}\}^3_{\mathrm{eq}} \{H_4SiO_4\}_{\mathrm{eq}} \{OH^-\}^6_{\mathrm{eq}} = 9.6 \cdot 10^{-23}$ is the equilibrium constant of C_3S [18], and Π is the ionic activity product in solution calculated accordingly.

As shown in Figure 9, the change of the dissolution rate was plotted as a function of $\ln\Pi(C_3S)$, and our experimental values of $\ln\Pi$ ranged from -90 to -50.7. The first corresponded to the level of undersaturation of the solution with respect to C_3S that can be reached at different times moving away from the solid-liquid interface along the z-axis of the holographic cell (see Figure 1),

while the second corresponded to the solubility of C_3S. Our curve provided a coherent view of the dissolution kinetics of C_3S, characterized by the dissolution plateau far from the equilibrium and the linear decrease of the dissolution rate when approaching the equilibrium. There are still discrepancies between the various experiments about the dissolution kinetics when moving toward the equilibrium. Methods with a flowing or stirred solution are less suitable for reaching so close-to-equilibrium conditions. The strength of our technique relies on the fact that dissolution proceeds in a quiescent solution. This absence of imposed stirring allowed the monitoring of a wide range of $\ln \Pi$ in the cell, primarily making our methodology particularly appropriate for close-to-equilibrium investigations. For this reason, we support that our dissolution law may provide reliable values close to the solubility of C_3S. Moreover, we would stress that this curve, which relies on the classic TST, may well describe the real dissolution kinetics of C_3S in consideration of the quality of the fitting of our datasets assuming a first-order reaction.

Further dissolution data available in the literature, from samples dissolved in deionized water or lime solution, were added in Figure 9. Dissolution rates higher than as set forth in our confidence interval (see upper bound marked with a black dashed line in Figure 9) were not included.

Nicoleau et al. [18], who resorted to batch experiments and ICP measurements, were the first ones to clearly exemplify the sigmoidal shape of the dissolution rate law of C_3S and ascribed it to the presence of etch pits. The data with the same $[CaO]_{aq}$ in the initial solution (5, 5.5, 8.5, 10.5, 11, and 15 mM) and a water-to-solid ratio of 10 were averaged and included in Figure 9. Juilland and Gallucci [13] performed VSI measurements on C_3S surfaces dissolved in solutions of different $[CaO]_{aq}$ concentration and back-calculated the saturation state of the reacted solutions from the amount of dissolved material. The data collected with the aid of a flow-through cell at fluxes of 9, 18, and 36 ml $\cdot min^{-1} \cdot mm^{-2}$ and having the same $[CaO]_{aq}$ in the initial solution (0, 2, 4.7, 7.85, 11.5, 15, 18, 20 mM) were averaged, normalized to zero-flow conditions by linear regression and included in Figure 9. Interestingly, in the experiments of

these last authors, dissolution rates from C_3S samples reacted in deionized water increased with the imposed flow rate and the rate at the dissolution plateau corresponded to 22.2 μmol·m^{-2}·s^{-1} at zero-flow, hence close to our k_{C3S}. Furthermore, dissolution rates of C_3S provided by other VSI measurements from Robin et al. [20] and Marchon et al. [21] were included in in Figure 9. It is worth noting that Robin et al. [20] have been able to evidence the discrepancy between the dissolution rate of various single crystal faces of C_3S and pointed out the non-monotonous shrinkage rate of the C_3S grains during their hydration. Therefore, given the dispersion of the rates measured along different C_3S orientations, just a few averaged values were shown in our figure.

Beyond the degree of undersaturation, empirical laws used to describe the dissolution of minerals may be expressed as a function of the solution pH and may take into account the dependency of the rate on the ionic strength of the solution and/or ion-specific effects [57, 18, 41, 50, 58].

Here, in light of the selected data from the literature, we furnished possible functions that can be used to describe the reduction of the dissolution rate of C_3S by approaching the equilibrium, assuming that our k_{C3S} was independent of the $[CaO]_{aq}$ concentration of the hydrating solution. In compliance with the TST and the dissolution theory by crystal lattice defects, we arranged Equation 7 by introducing fitting parameters with the aim of providing empirical laws for the fitting of the data from the literature.

According to Equation 8, a TST-based curve with $n = 0.2$ was shown in Figure 9, in order to highlight how this single exponent may vary the dissolution path. For example, a similar rate law was adopted in the study of the dissolution of albite [53], and, in that case, the n-parameter was varied from 0.1 to 0.5. Sigmoidal curves were then obtained by the adjustment of both the fitting parameters n and m. In particular, the m-parameter was varied to describe the non-linear dependency of the dissolution rate when approaching equilibrium due to the control of crystal defects at the interface [54, 55, 56]. We observed that the dataset from Nicoleau et al. [18] and the one from Juilland and Gallucci [13] follow approximately the same trend and their close-to-equilibrium dissolution

rates were empirically described by acting on the m-parameter.

$$R = k_{\mathrm{C3S}} \cdot \left(1 - \left(\frac{\Pi}{K_{\mathrm{eq}}}\right)^{n}\right)^{m} \tag{8}$$

The sigmoidal fashion predicts that the dissolution of C_3S is controlled by pre-existing lattice defects that may drive the dissolution rate from higher levels of undersaturation than what is predicted by using the TST formulation. Reducing the gap between the rates determined in literature with different methods, as well as the uncertainty associated with the computation of the activity of ionic species, may help in providing the optimal combination of fitting parameters. However, we would stress that, from a physical standpoint, these parameters should be implemented in the solution of Fick's equation (see Equation 2) to be properly estimated along with the value of k. This strategy turns into considering a higher reaction rate order, but this choice was discarded in light of the quality of our data fitting.

At present, the availability of experimental techniques to determine pure constants of reaction is still limited. Holographic interferometry may provide reliable data on mineral phases, and previous implementations of this technique led to uncertainties on the dissolution rates lower than 15%, i.e., much lower than standard dissolution methods [22]. The two main advantages of holographic interferometry for the study of dissolution are the ability to carry out measurements with no flux imposed and to access in real-time the concentration field in the solution. The corresponding drawbacks lie in the fact that the technique is purely optical, and does not provide any chemical analysis. For this reason, the computation of the concentration of the solution from its change of index of refraction requires strong assumptions based on validating observation techniques, like SEM, and chemical analyses, like ICP-AES. The application of holographic interferometry is particularly convenient when the mineral present a simple stoichiometry and the surface is not affected by multiple reactions. In the present study, as two reactions were occurring simultaneously, a careful

analysis of the data, including speciation calculations, was carried out to deduce correctly the dissolution rate from the concentration field. Therefore, the processing of the optical data, resting on complementary techniques, makes this methodology less straightforward for the study of cement hydration than, for instance, for the study of gypsum dissolution.

4. Conclusions

Accurate measurements of the dissolution rate are needed in order to interpret the hydration of C_3S. In this study, we turned to an unconventional optical technique with the aim of determining the dissolution rate constant of the C_3S phase in water and tiny quantities of $[CaO]_{aq}$ in the initial solution. The experiments were carried out in supersaturated conditions with respect to C–S–H and below the saturation of CH. A flat surface of C_3S was monitored in a quiescent solution. We related the variation of the index of refraction to the concentration of calcium ions released within the holographic cell and, with attention to previous studies [37, 44], we constrained the aqueous solution composition to the C–S–H stoichiometry at the interface. The pure dissolution rate constant of the C_3S phase was determined: $k_{C3S} = (19.8 \pm 4.4)\ \mu mol{\cdot}m^{-2}{\cdot}s^{-1}$. This rate corresponds to the rate at far-from-equilibrium conditions, hence not affected by the variation of the saturation state. Interestingly, the rate constant obtained by the holographic interferometry study, which quantified interfacial concentrations, was in close agreement with rates determined by topographic investigations [41]. The variation of the dissolution rate towards the equilibrium was obtained from our experiments with the rate law: $R = k_{C3S}(1-\Pi/K_{eq})$. To strengthen the consensus toward this new protocol, further details on interfacial pH, saturation index of the phases, and precipitation of the C–S–H phase during our experiments were provided. We encourage the use of our thermodynamic constant on stochastic simulations to model cement hydration kinetics.

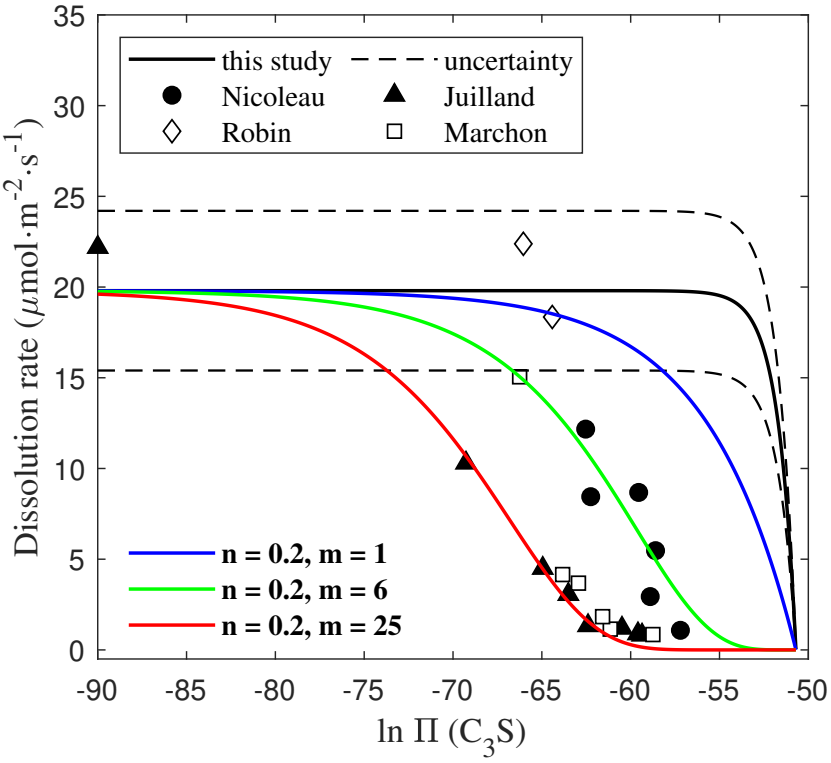

Figure 9: Dissolution rate of C_3S as a function of the natural logarithm of the ionic activity product of the solution ($Ca_3SiO_5 + 5H_2O \rightarrow 3Ca^{2+} + H_4SiO_4 + 6OH^-$). The black solid line represents the dissolution of C_3S in deionized water and is a non-sigmoidal function complying with TST (black dashed lines below and above display the experimental uncertainty due to the standard deviation on the rate constant k_{C3S}. Blue circles: data from Nicoleau et al. [18] and collected in a reactor connected to an ICP spectrometer. The data with the same $[CaO]_{aq}$ into the initial solution (5, 5.5, 8.5, 10.5, 11 and 15 mM) and w/s = 10 were averaged. Black triangles: data from Juilland and Gallucci [13] collected with the aid of a a flow-through-cell and VSI measurements. White diamonds: data from Robin et al. [20]. White squares: data from Marchon et al. [21]. Functions including n and m parameters were added in different colors.

References

[1] E. Durgun, H. Manzano, R. Pellenq, J. C. Grossman, Understanding and controlling the reactivity of the calcium silicate phases from first principles, Chemistry of Materials 24 (7) (2012) 1262–1267.

[2] Y. Li, H. Ai, K. H. Lo, Y. Kong, H. Pan, Z. Li, Insight into adsorption mechanism of water on tricalcium silicate from first-principles calculations, Cement and Concrete Research 152 (2022) 106684.

[3] C. Qi, L. Liu, J. He, Q. Chen, L.-J. Yu, P. Liu, Understanding cement hydration of cemented paste backfill: DFT study of water adsorption on tricalcium silicate (111) surface, Minerals 9 (4) (2019) 202.

[4] E. Pustovgar, R. P. Sangodkar, A. S. Andreev, M. Palacios, B. F. Chmelka, R. J. Flatt, J.-B. dEspinose de Lacaillerie, Understanding silicate hydration from quantitative analyses of hydrating tricalcium silicates, Nature communications 7 (1) (2016) 1–9.

[5] J. Claverie, F. Bernard, J. M. M. Cordeiro, S. Kamali-Bernard, Water's behaviour on Ca-rich tricalcium silicate surfaces for various degrees of hydration: A molecular dynamics investigation, Journal of Physics and Chemistry of Solids 132 (2019) 48–55.

[6] I. G. Richardson, The calcium silicate hydrates, Cement and concrete research 38 (2) (2008) 137–158.

[7] D. A. Kulik, Improving the structural consistency of C–S–H solid solution thermodynamic models, Cement and Concrete Research 41 (5) (2011) 477–495.

[8] E. Gartner, I. Maruyama, J. Chen, A new model for the C–S–H phase formed during the hydration of Portland cements, Cement and Concrete Research 97 (2017) 95–106.

[9] R. Feldman, P. Sereda, A new model for hydrated Portland cement and its practical implications, Engineering Journal 53 (8-9) (1970) 53–59.

[10] A. J. Allen, J. J. Thomas, H. M. Jennings, Composition and density of nanoscale calcium–silicate–hydrate in cement, Nature materials 6 (4) (2007) 311–316.

[11] S. Garrault, A. Nonat, Hydrated layer formation on tricalcium and dicalcium silicate surfaces: experimental study and numerical simulations, Langmuir 17 (26) (2001) 8131–8138.

[12] Lasaga, Antonio C and Lüttge, Andreas, Variation of crystal dissolution rate based on a dissolution stepwave model, Science 291 (5512) (2001) 2400–2404.

[13] P. Juilland, E. Gallucci, Morpho-topological investigation of the mechanisms and kinetic regimes of alite dissolution, Cement and Concrete Research 76 (2015) 180–191.

[14] J. Xu, C. Fan, H. H. Teng, Calcite dissolution kinetics in view of Gibbs free energy, dislocation density, and pCO_2, Chemical Geology 322 (2012) 11–18.

[15] O. S. Pokrovsky, S. V. Golubev, J. Schott, Dissolution kinetics of calcite, dolomite and magnesite at 25°C and 0 to 50 atm pCO_2, Chemical geology 217 (3-4) (2005) 239–255.

[16] M. D. Vinson, A. Lüttge, Multiple length-scale kinetics: an integrated study of calcite dissolution rates and strontium inhibition, American Journal of Science 305 (2) (2005) 119–146.

[17] J. Colombani, Dissolution measurement free from mass transport, Pure and Applied Chemistry 85 (1) (2012) 61–70.

[18] L. Nicoleau, A. Nonat, D. Perrey, The di-and tricalcium silicate dissolutions, Cement and Concrete Research 47 (2013) 14–30.

[19] F. Bellmann, T. Sowoidnich, H.-M. Ludwig, D. Damidot, Dissolution rates during the early hydration of tricalcium silicate, Cement and Concrete Research 72 (2015) 108–116.

[20] V. Robin, B. Wild, D. Daval, M. Pollet-Villard, A. Nonat, L. Nicoleau, Experimental study and numerical simulation of the dissolution anisotropy of tricalcium silicate, Chemical Geology 497 (2018) 64–73.

[21] D. Marchon, P. Juilland, E. Gallucci, L. Frunz, R. J. Flatt, Molecular and submolecular scale effects of comb-copolymers on tri-calcium silicate reactivity: Toward molecular design, Journal of the American Ceramic Society 100 (3) (2017) 817–841.

[22] E. A. Pachon-Rodriguez, J. Colombani, Pure dissolution kinetics of anhydrite and gypsum in inhibiting aqueous salt solutions, AIChE Journal 59 (5) (2013) 1622–1626.

[23] H. Gay, T. Meynet, J. Colombani, Local study of the corrosion kinetics of hardened Portland cement under acid attack, Cement and Concrete Research 90 (2016) 36–42.

[24] F. Sorrentino, Upscaling the synthesis of tricalcium silicate and alite, Cement Wapno Beton 8 (2008) 177–183.

[25] A. S. Brand, J. W. Bullard, Dissolution kinetics of cubic tricalcium aluminate measured by digital holographic microscopy, Langmuir 33 (38) (2017) 9645–9656.

[26] A. S. Brand, J. M. Gorham, J. W. Bullard, Dissolution rate spectra of β-dicalcium silicate in water of varying activity, Cement and Concrete Research 118 (2019) 69–83.

[27] J. Colombani, J. Bert, Holographic visualization of convection during thermotransport: application to microgravity experiments, Measurement Science and Technology 10 (10) (1999) 886.

[28] J. Colombani, J. Bert, Holographic interferometry study of the dissolution and diffusion of gypsum in water, Geochimica et cosmochimica acta 71 (8) (2007) 1913–1920.

[29] J. J. Thomas, A new approach to modeling the nucleation and growth kinetics of tricalcium silicate hydration, Journal of the American Ceramic Society 90 (10) (2007) 3282–3288.

[30] L. Valentini, M. Favero, M. C. Dalconi, V. Russo, G. Ferrari, G. Artioli, Kinetic model of calcium-silicate hydrate nucleation and growth in the presence of PCE superplasticizers, Crystal Growth & Design 16 (2) (2016) 646–654.

[31] S. Garrault-Gauffinet, A. Nonat, Experimental investigation of calcium silicate hydrate (CSH) nucleation, Journal of crystal growth 200 (3-4) (1999) 565–574.

[32] L. Nicoleau, M. A. Bertolim, Analytical model for the alite (C_3S) dissolution topography, Journal of the American Ceramic Society 99 (3) (2016) 773–786.

[33] B. Mota, J. E. Rossen, Karen Scrivener, Amélie Bazzoni, A Practical Guide to Microstructural Analysis of Cementitious Materials (2018) 351.

[34] L. Nicoleau, A. Nonat, A new view on the kinetics of tricalcium silicate hydration, Cement and Concrete Research 86 (2016) 1–11.

[35] A. K. Mohamed, S. C. Parker, P. Bowen, S. Galmarini, An atomistic building block description of C–S–H - Towards a realistic C–S–H model, Cement and Concrete Research 107 (2018) 221–235.

[36] I. G. Richardson, The nature of C–S–H in hardened cements, cement and concrete research 29 (8) (1999) 1131–1147.

[37] J. W. Bullard, G. W. Scherer, An ideal solid solution model for C–S–H, Journal of the American Ceramic Society 99 (12) (2016) 4137–4145.

[38] J. J. Chen, J. J. Thomas, H. F. Taylor, H. M. Jennings, Solubility and structure of calcium silicate hydrate, Cement and concrete research 34 (9) (2004) 1499–1519.

[39] J. Haas, A. Nonat, From C–S–H to C–A–S–H: Experimental study and thermodynamic modelling, Cement and Concrete Research 68 (2015) 124–138.

[40] J. P. Gustafsson, Visual MINTEQ 3.0 user guide, KTH, Department of Land and Water Recources, Stockholm, Sweden.

[41] A. Kumar, J. Reed, G. Sant, Vertical scanning interferometry: a new method to measure the dissolution dynamics of cementitious minerals, Journal of the American Ceramic Society 96 (9) (2013) 2766–2778.

[42] P. Juilland, E. Gallucci, R. Flatt, K. Scrivener, Dissolution theory applied to the induction period in alite hydration, Cement and Concrete Research 40 (6) (2010) 831–844.

[43] P. Juilland, L. Nicoleau, R. S. Arvidson, E. Gallucci, Advances in dissolution understanding and their implications for cement hydration, RILEM Technical Letters 2 (2017) 90–98.

[44] P. Blanc, X. Bourbon, A. Lassin, E. C. Gaucher, Chemical model for cement-based materials: Temperature dependence of thermodynamic functions for nanocrystalline and crystalline C–S–H phases, Cement and Concrete Research 40 (6) (2010) 851–866.

[45] A. Behnood, K. Van Tittelboom, N. De Belie, Methods for measuring pH in concrete: A review, Construction and Building Materials 105 (2016) 176–188.

[46] B. Lothenbach, F. Winnefeld, C. Alder, E. Wieland, P. Lunk, Effect of temperature on the pore solution, microstructure and hydration products of Portland cement pastes, Cement and Concrete Research 37 (4) (2007) 483–491.

[47] B. Lothenbach, G. Le Saout, E. Gallucci, K. Scrivener, Influence of limestone on the hydration of Portland cements, Cement and Concrete Research 38 (6) (2008) 848–860.

[48] F. Bellmann, G. W. Scherer, Analysis of C–S–H growth rates in supersaturated conditions, Cement and Concrete Research 103 (2018) 236–244.

[49] J. W. Bullard, A three-dimensional microstructural model of reactions and transport in aqueous mineral systems, Modelling and Simulation in Materials Science and Engineering 15 (7) (2007) 711.

[50] J. W. Bullard, A determination of hydration mechanisms for tricalcium silicate using a kinetic cellular automaton model, Journal of the American Ceramic Society 91 (7) (2008) 2088–2097.

[51] M. S. Beig, A. Lüttge, Albite dissolution kinetics as a function of distance from equilibrium: Implications for natural feldspar weathering, Geochimica et Cosmochimica Acta 70 (6) (2006) 1402–1420.

[52] R. S. Arvidson, A. Luttge, Mineral dissolution kinetics as a function of distance from equilibrium–New experimental results, Chemical geology 269 (1-2) (2010) 79–88.

[53] T. Burch, K. Nagy, A. Lasaga, Free energy dependence of albite dissolution kinetics at 80°C and pH 8.8, Chemical Geology 105 (1-3) (1993) 137–162.

[54] R. Shiraki, S. L. Brantley, Kinetics of near-equilibrium calcite precipitation at 100°C: An evaluation of elementary reaction-based and affinity-based rate laws, Geochimica et Cosmochimica Acta 59 (8) (1995) 1457–1471.

[55] J. W. Morse, R. S. Arvidson, A. Lüttge, Calcium carbonate formation and dissolution, Chemical reviews 107 (2) (2007) 342–381.

[56] S. L. Brantley, Kinetics of mineral dissolution, in: Kinetics of water-rock interaction, Springer, 2008, pp. 151–210.

[57] D. Damidot, F. Bellmann, T. Sovoidnich, B. Möser, Measurement and simulation of the dissolution rate at room temperature in conditions close to a cement paste: from gypsum to tricalcium silicate, Journal of Sustainable Cement-Based Materials 1 (3) (2012) 94–110.

[58] J. W. Bullard, G. W. Scherer, J. J. Thomas, Time dependent driving forces and the kinetics of tricalcium silicate hydration, Cement and Concrete Research 74 (2015) 26–34.

[59] X. Li, Q. Hu, B. Robertson, M. T. Ley, V. J. De Andrade, G. Sokhansefat, Direct observation of C_3S particle dissolution using fast nano X-ray computed tomography, Cement and Concrete Research 166 (2023) 107097.

[60] J. Neubauer, T. Sowoidnich, L. Valentini, C. Schulbert, C. Naber, C. Rößler, J. DaSilva, F. Bellmann, Evolution of the particle size distribution of tricalcium silicate during hydration by synchrotron X-ray nanotomography, Cement and Concrete Research 156 (2022) 106769.

[61] S. Shirani, A. Cuesta, A. Morales-Cantero, I. Santacruz, A. Diaz, P. Trtik, M. Holler, A. Rack, B. Lukic, E. Brun, et al., 4D nanoimaging of early age cement hydration, Nature Communications 14 (1) (2023) 2652.